ADVANCED MATERIALS

Supporting Information

for *Adv. Mater.*, DOI: 10.1002/adma.201505775

Cluster-Mediated Crossed Bilayer Precision Assemblies of 1D Nanowires

Anirban Som, *Indranath Chakraborty*, *Tuhina Adit Maark*, *Shridevi Bhat*, and *Thalappil Pradeep**

Supporting Information

Cluster Mediated Crossed Bilayer Precision Assemblies of 1D Nanowires

*Anirban Som, Indranath Chakraborty, Tuhina Adit Maark, Shridevi Bhat and Thalappil Pradeep **

Table of contents

List of figures

Chemicals used

All the chemicals were commercially available and were used without further purification. Silver nitrate ($AgNO_3$, 99%), gold (III) chloride trihydrate ($HAuCl_4$, $3H_2O$, 99%), 4-mercaptobenzoic acid (MBA, 97%) and sodium borohydride ($NaBH_4$, 99.99%) were purchased from Aldrich. Tellurium dioxide (TeO_2, 99.9%) powder, hydrazine monohydrate ($N_2H_4.H_2O$, 99-100%) and PVP (Polyvinylpyrrolidone, K25) were supplied by Alfa Aesar, Fischer Scientific and SD Fine Chemicals, respectively. Ethylene glycol (LR), dimethylformamide (DMF, AR grade), dimethysulfoxide (DMSO, AR grade), toluene (AR grade), methanol (AR grade), ammonium acetate, citric acid and sodium hydroxide (NaOH) pellets were procured from RANKEM, India

Computational modeling

The structure for $Ag_{44}(MBA)_{30}$ was generated using the X-ray crystallographic coordinates deposited at the Cambridge Crystallographic Data Centre (CCDC) under the deposition name CCDC 949240. This data is available free of charge from CCDC at http://www.ccdc.cam.ac.uk/data_request/cif. To model the Te NW bilayer assembly (parallel and orthogonal), the Ag_{44} clusters were sandwiched between Te(001) surfaces. All the structures were built using ase-gui, which is the graphical interface available with Atomic Simulation Environment (ASE)[1], and VESTA[2] visualization software program.

Supporting Information Figures

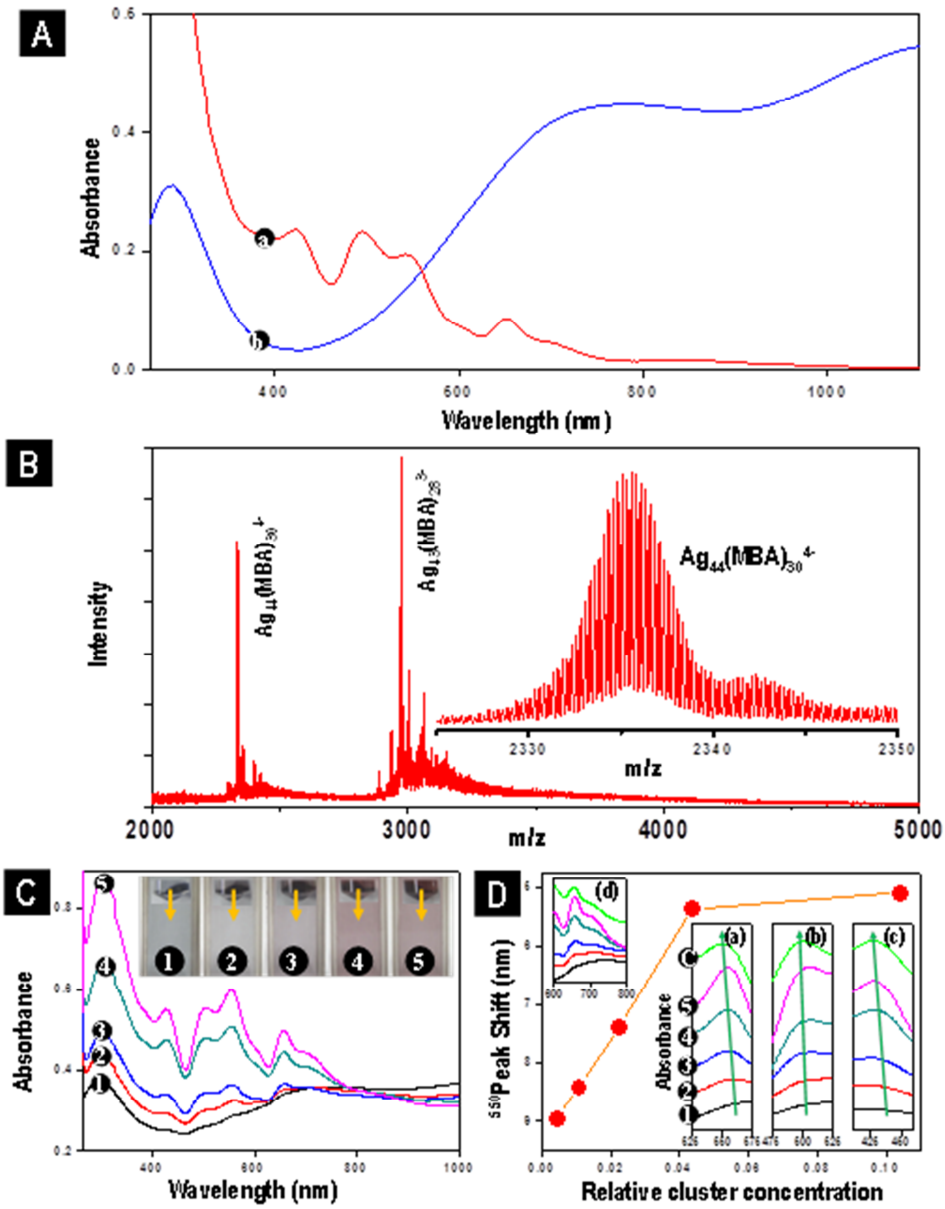

Figure S1. A) UV-visible absorption spectra of a) Ag_{44}(p-MBA)$_{30}$ and b). Te NWs. B) ESI mass spectrum of Ag_{44}(p-MBA)$_{30}$. Expanded view of molecular ion peak (4 –ve charge) is shown in the inset along with the theoretical spectrum of the same ion. Minor features are due to fragments or association products during ionization. C) UV-vis absorption spectra of Ag_{44}@Te NWs with increasing cluster concentration (C_1-C_5, marked with 1 to 5). The NWs after cluster attachment were precipitated out through centrifugation and re-dispersed prior to the measurement of the spectra. Images of the procedure are shown in the inset. D) Shift of the 550 nm peak of Ag_{44} is plotted with increasing cluster concentration at a fixed Te NW concentration. Peak shift decreases with increasing concentration, indicating multilayer adsorption of clusters on Te NW surface at higher concentration. Gradual changes in positions of different peaks of Ag_{44} are shown in the insets.

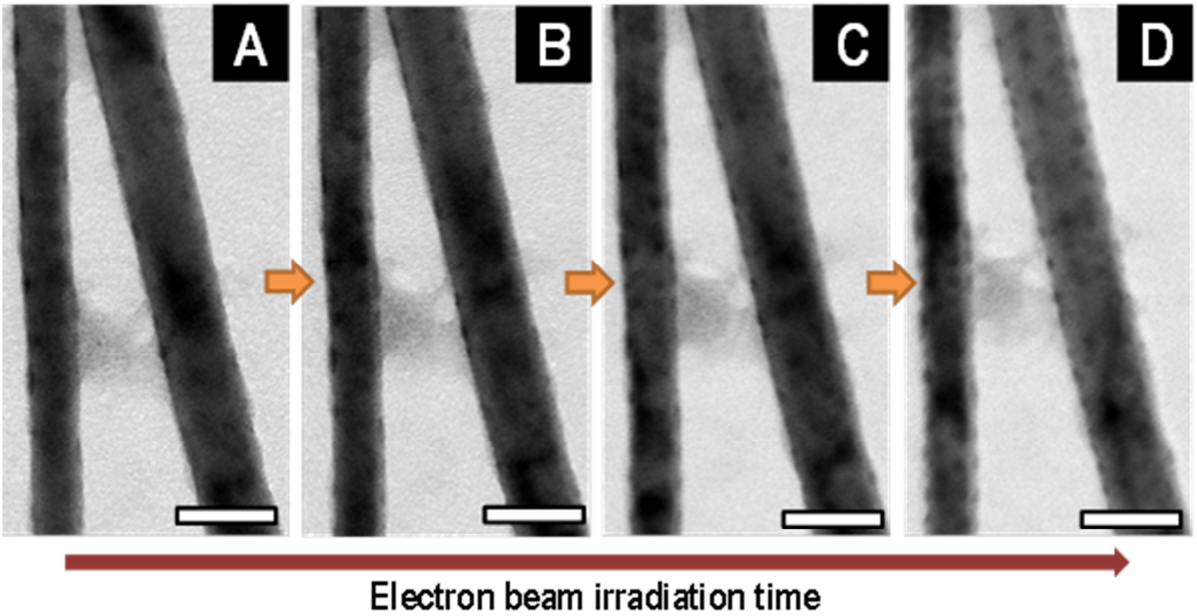

Figure S2. TEM images showing time evolution of nodules upon electron beam irradiation of Ag_{44}@Te NWs (C_3). Image A was acquired immediately. Subsequent images were acquired following a 30 s electron beam irradiation. The scale bar is 50 nm for all the images.

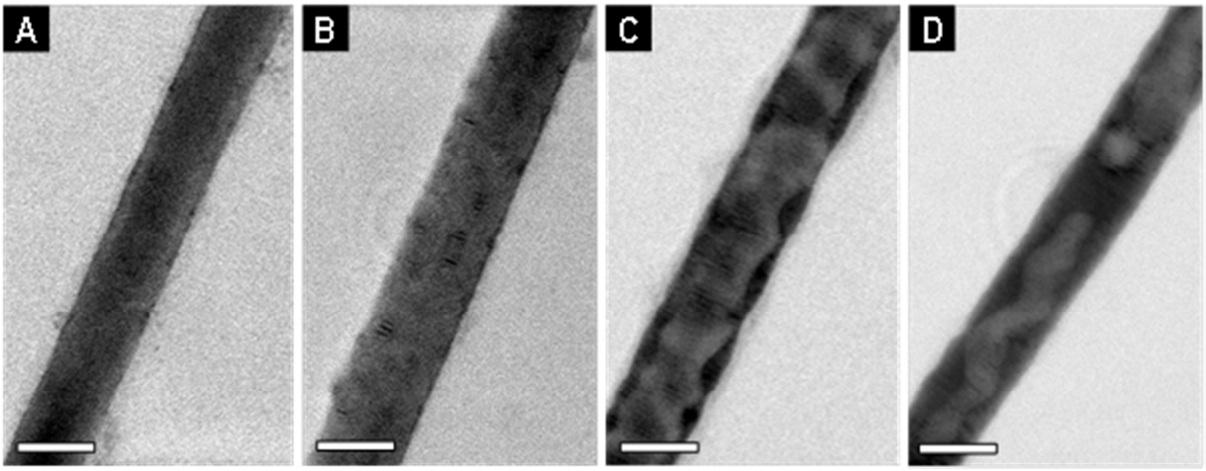

Figure S3. TEM images of Ag_{44}@Te NWs at different loadings of Ag_{44}, showing the size and the extent of nodule/island coverage of the NWs; (A) C_1, (B) C_2, (C) C_4 and (D) C_5. Scale bar is 20 nm in all the images.

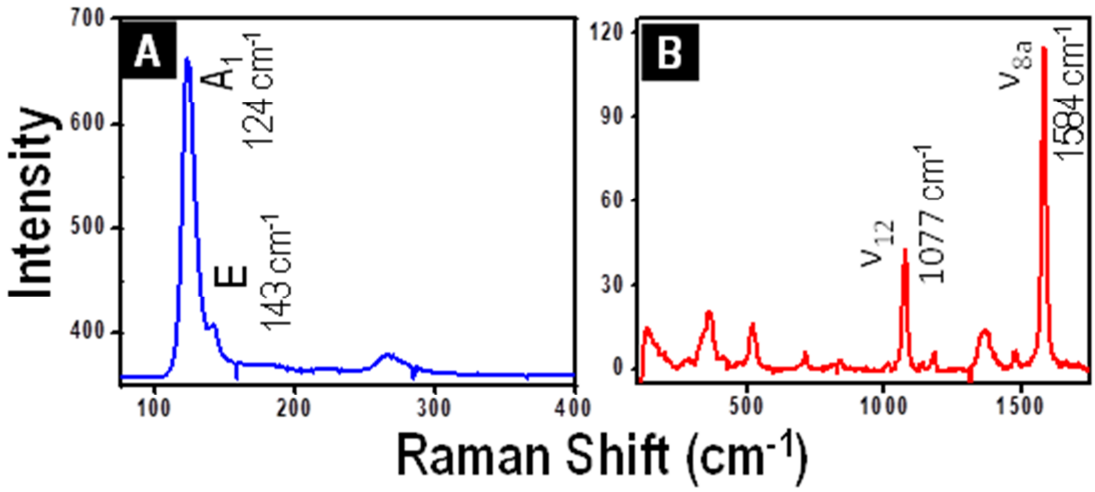

Figure S4. (A) Raman spectra of Te NWs. The most intense Raman peak at 124 cm^{-1} is due to the Raman active singlet A1 mode of Te lattice vibrations, while the less intense peak at 143 cm^{-1} is one of the E doublets. (B) Raman spectrum of Ag_{44}. The cluster is Raman active due to the Raman active nature of its protecting ligand (p-MBA). Two strong bands observed at 1077 and 1584 cm^{-1} arise from ν_{12} and ν_{8a} aromatic ring vibrations of p-MBA, respectively.

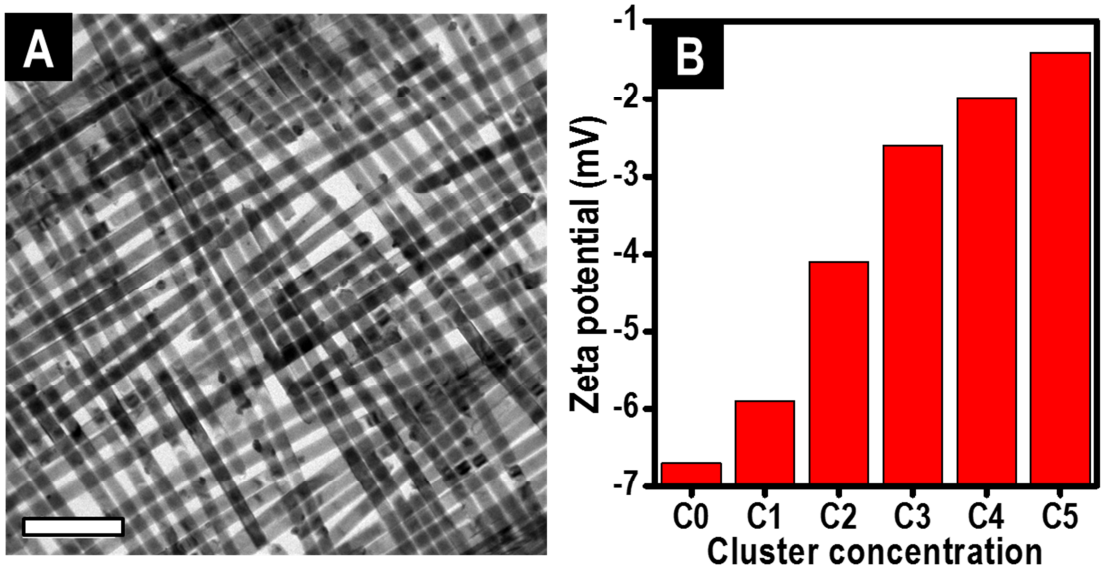

Figure S5. (A) Organized structure formed from butanolic dispersion of Ag_{44}@Te NWs (C_3) after solvent evaporation. (B) Increase in the value of zeta potential with increasing cluster loading. Scale bar in A is 200 nm.

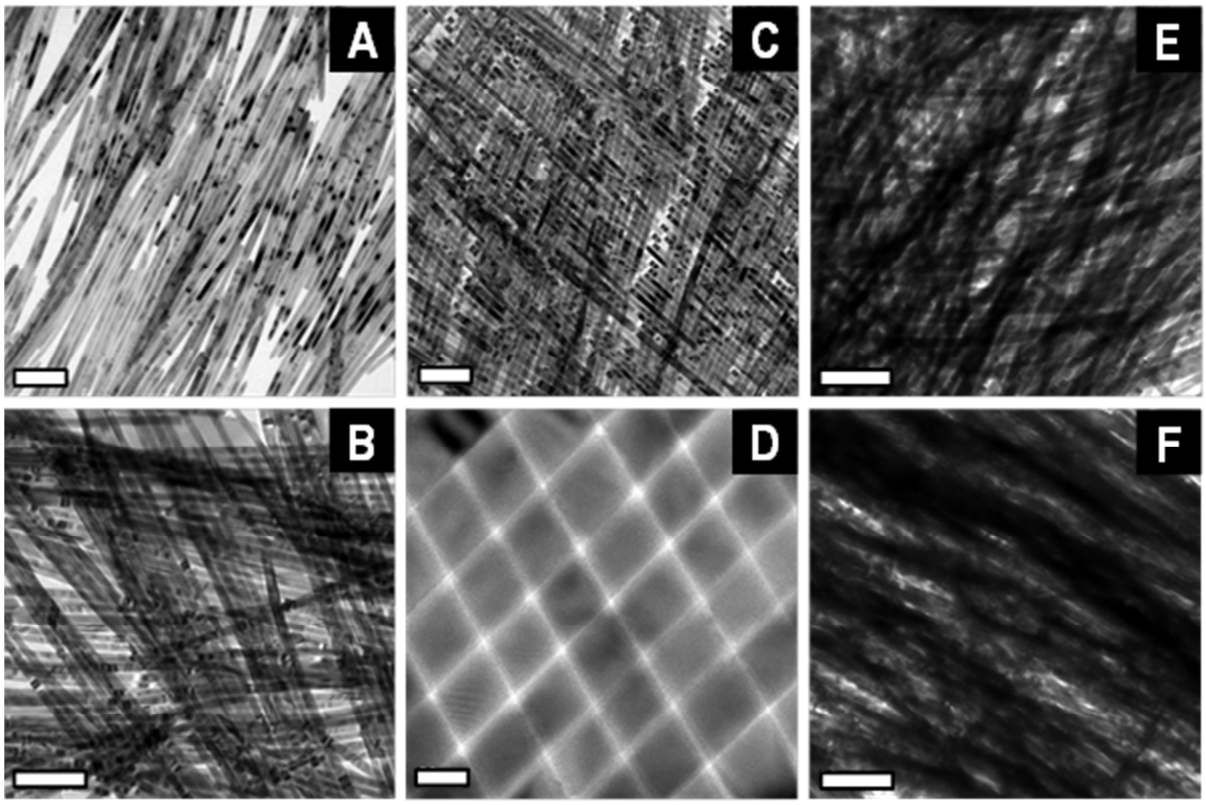

Figure S6. TEM images of the kind of Ag_{44}@Te NWs assemblies formed at different loading of Ag_{44}; (A) C_1, (B) C_2 (C) C_3, (E) C_4, (F) C_5. An area having perfect order from C_3 is expanded and shown in (D). Scale bar in D is 20 nm and is 200 nm for the other images.

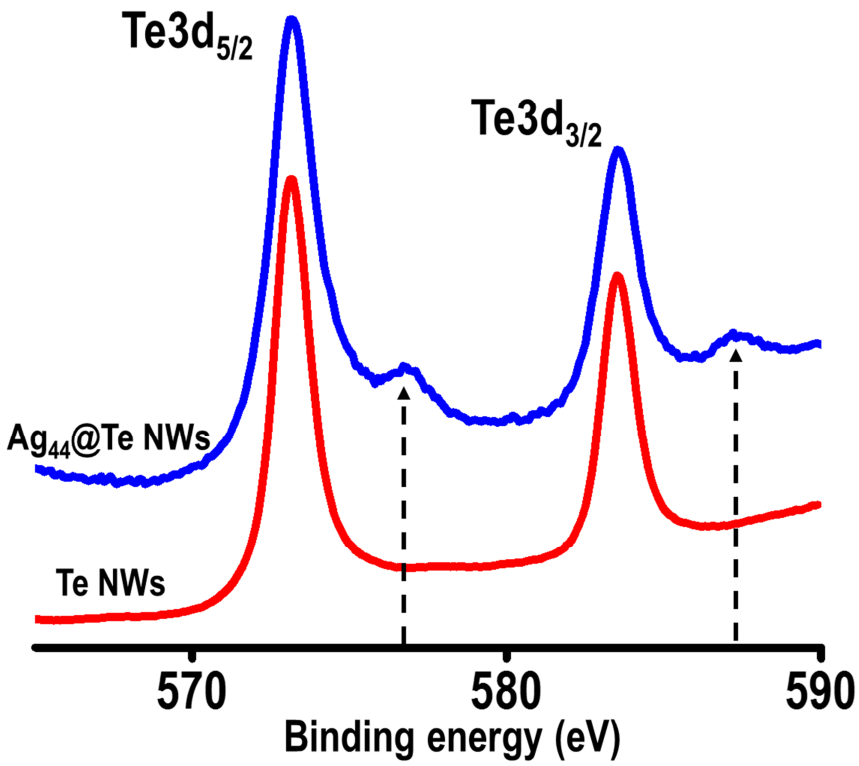

Figure S7. XPS spectra of the Te 3d region for Te (red trace) and Ag_{44}@Te (blue trace) NWs.

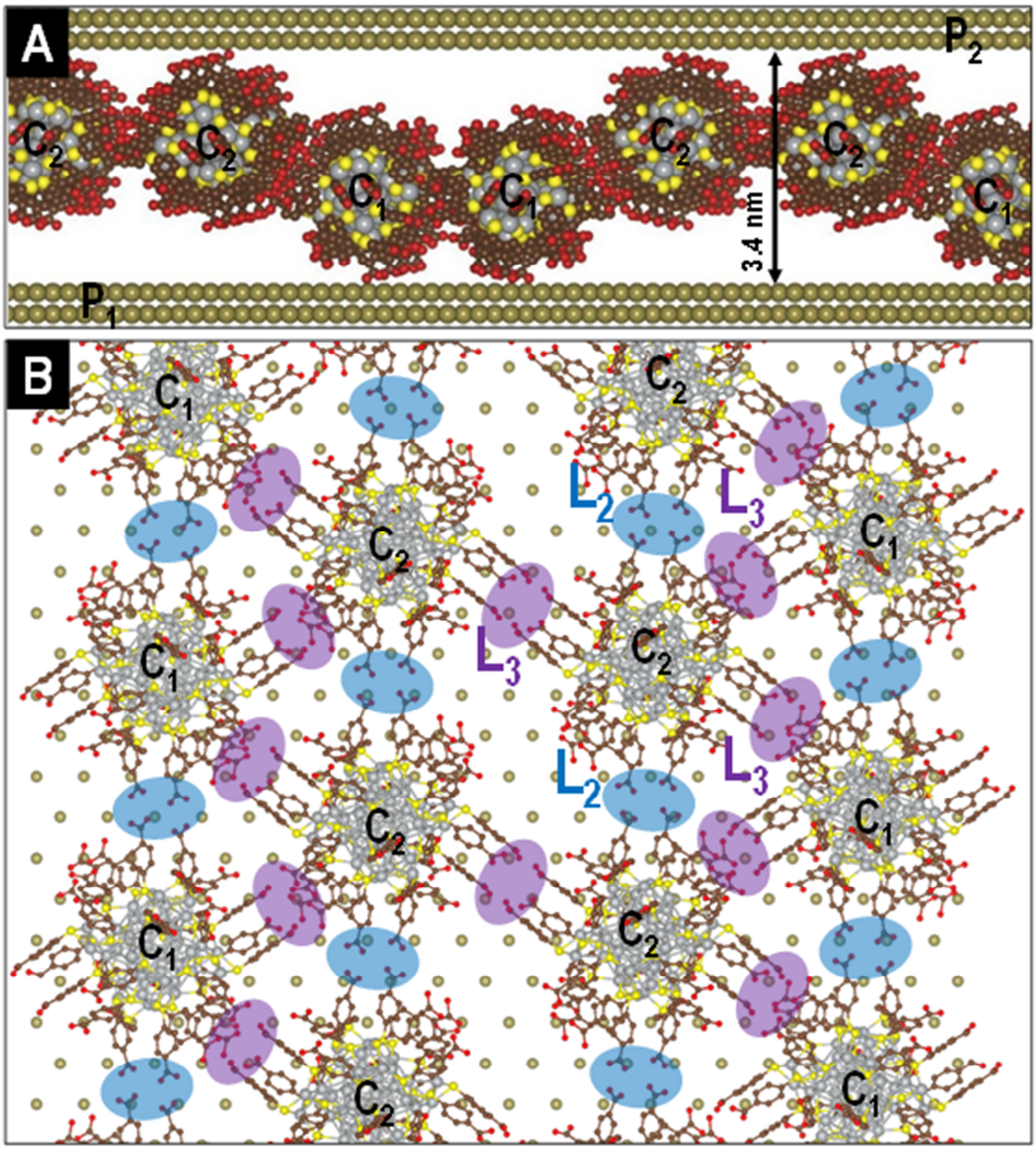

Figure S8. (A) Side view of Ag_{44} clusters sandwiched between two parallel Te surfaces. (B) Top view of the same showing H-bonded network of Ag_{44} clusters. Each cluster is surrounded by four clusters from the same plane and by two clusters from the second plane forming 13 H-bonds.

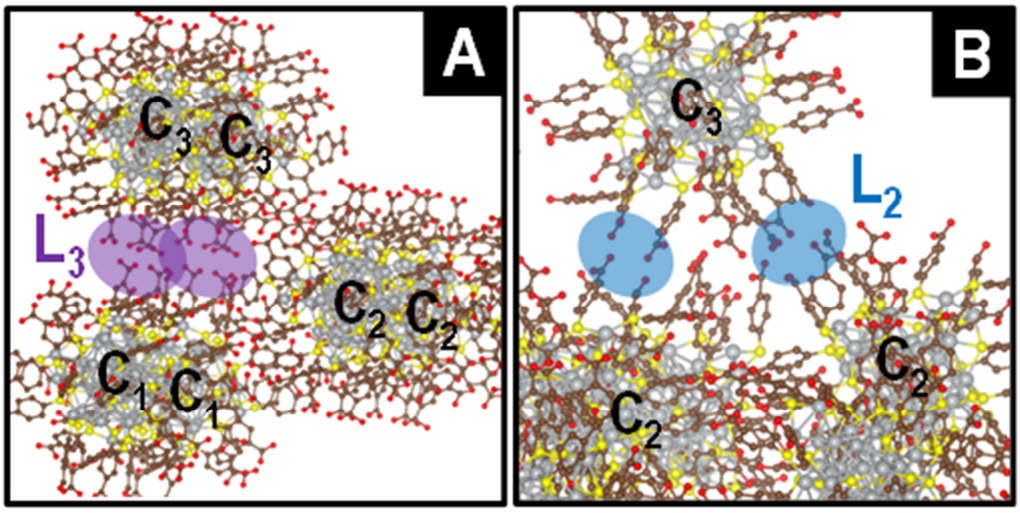

Figure S9. Zoomed in view of the Ag_{44} clusters in 81° orthogonal arrangement showing the formation of additional H-bonds, (A) L_3 H-bonds between C_3 and C_1 and (B) L_2 H-bonds between C_2 and C_1.

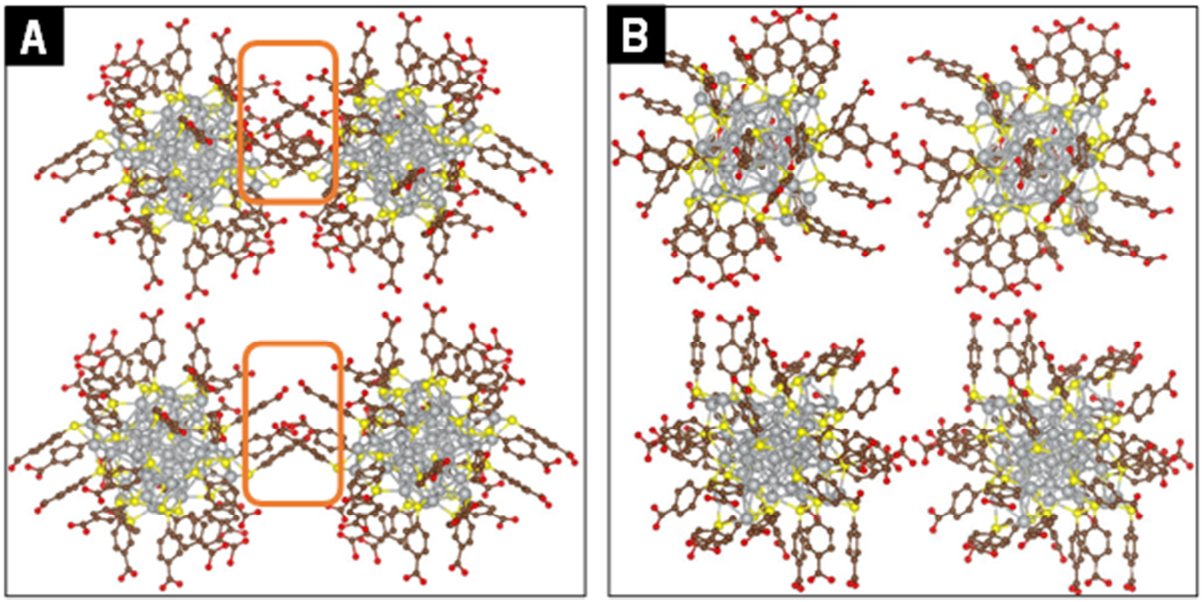

Figure S10. (A) Steric interactions between the neighboring clusters (marked) in 90° orthogonal arrangement. (B) Those interactions diminish in 81° orthogonal arrangement.

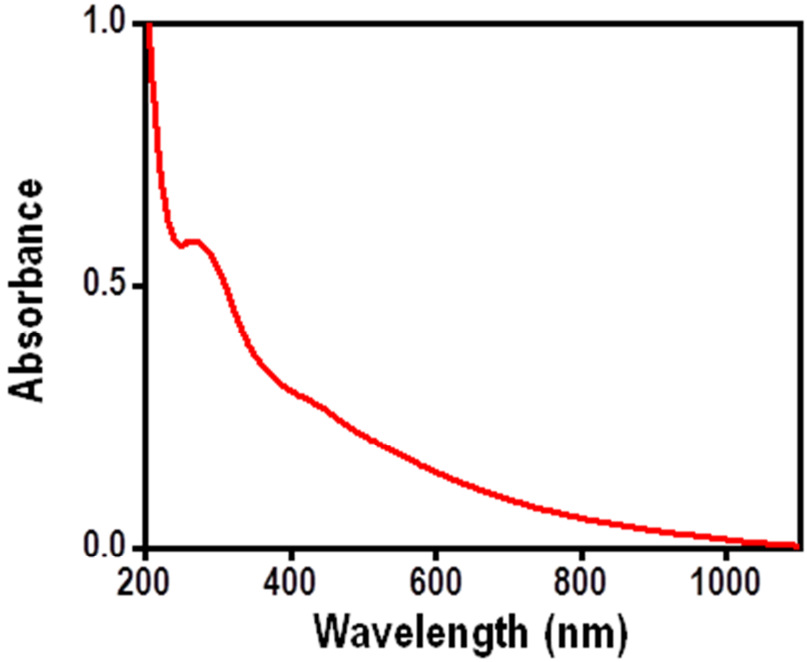

Figure S11. (A) UV-visible absorption spectrum of Au_{102} in water.

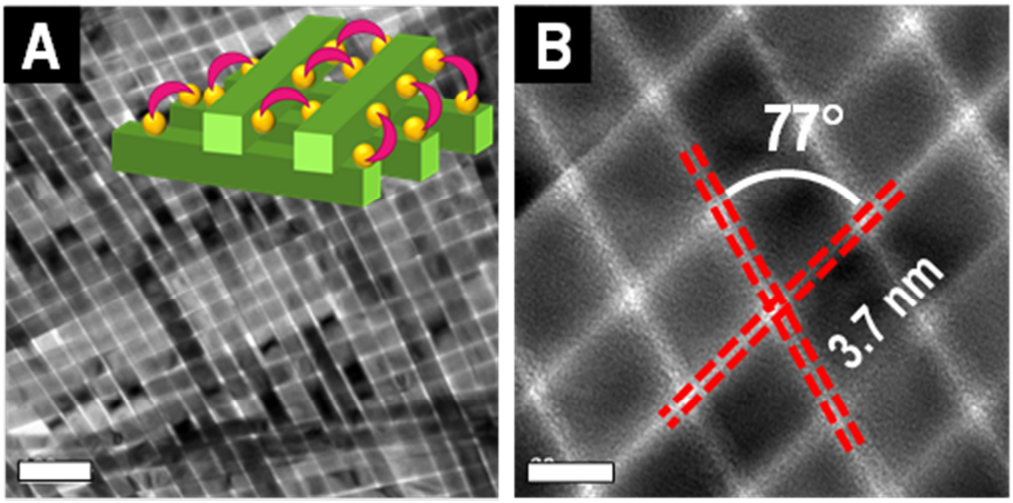

Figure S12. (A) TEM image of the orthogonal assembly formed form Au_{102}@Te NWs. A schematic representation of the assembly formation by inter-cluster H-bonding is shown in the inset. (B) Expanded view of the same assembly showing an inter NW distance of 3.7 nm and an interlayer NW angle of 77°. Scale bar is 100 nm in A and is 20 nm in B.

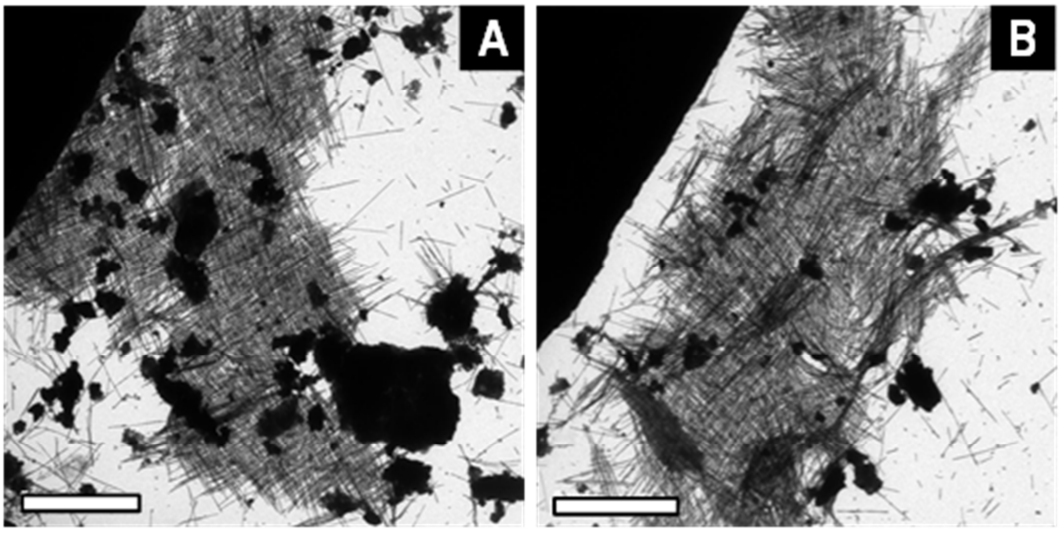

Figure S13. TEM images of orthogonal assembly formed after a dilute dispersion of Au_{102}@Te NWs was allowed to dry on the TEM grid. The system preferentially forms bilayers. Scale bar is 5 µm in both the images.

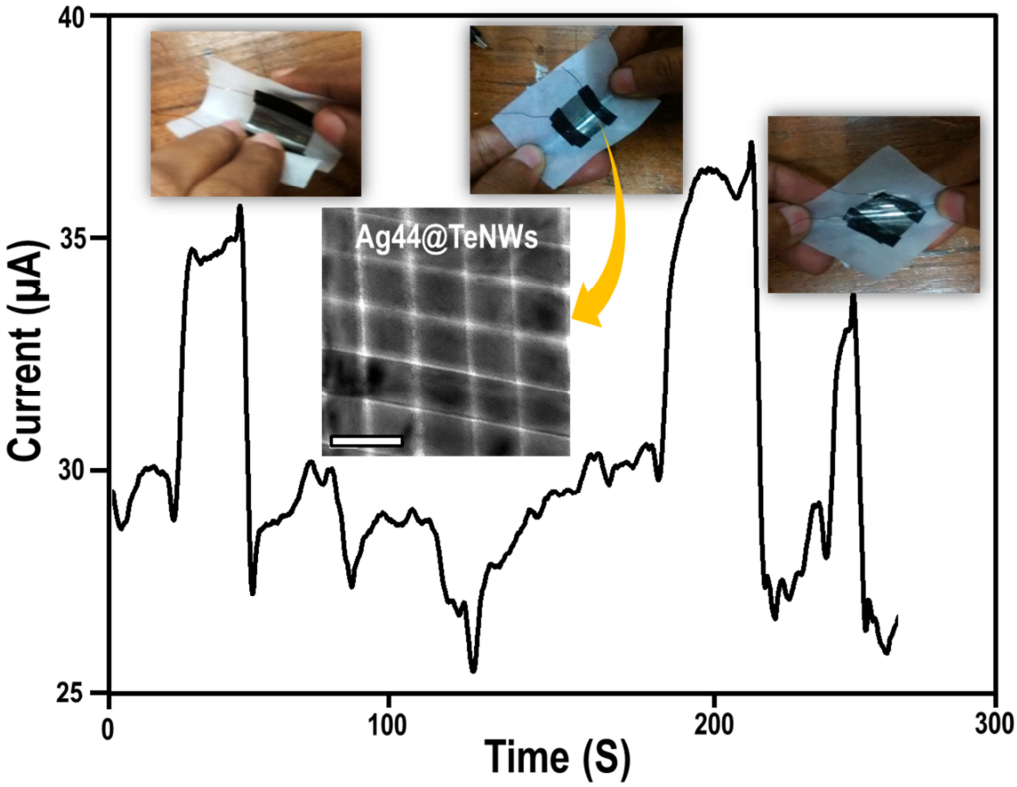

Figure S14. Change in the conductivity of the device made by transferring the crossed bilayer assembly of Ag_{44}@Te NWs on PET substrate.

References

(1) S. R. Bahn and K. W. Jacobsen, Comput. Sci. Eng. 2002, 5, 56-66.

(2) K. Momma and F. Izumi, J. Appl. Cryst. 2011, 44, 1272-1276. Code available at http://jp-minerals.org/vesta/en/